Summer 2018

Computational investigation of polymer electrolyte membrane fuel cell with nature-inspired Fibonacci spiral flow field

Suleyman Kose

Follow this and additional works at: https://scholarsmine.mst.edu/masters_theses

Part of the Mechanical Engineering Commons

Department:

Recommended Citation

COMPUTATIONAL INVESTIGATION OF POLYMER ELECTROLYTE

MEMBRANE FUEL CELL WITH NATURE-INSPIRED FIBONACCI SPIRAL FLOW

FIELD

by

SULEYMAN KOSE

A THESIS

Presented to the Faculty of the Graduate School of the

MISSOURI UNIVERSITY OF SCIENCE AND TECHNOLOGY

In Partial Fulfillment of the Requirements for the Degree

MASTER OF SCIENCE IN MECHANICAL ENGINEERING

2018

Approved by

Umit O. Koylu, Advisor
Kelly O. Homan
Ming C. Leu

ABSTRACT

Polymer electrolyte membrane fuel cells (PEMFC) are promising clean energy devices. The flow field design has crucial role in PEMFC performance for effective distribution of reactants and removal of products. Several nature-inspired flow field designs have recently been proposed in the literature. Common characteristics of these designs were sudden changes in the flow direction through sharp bends and flow field geometries restrained to areas having corners. In this thesis, Fibonacci spiral configuration, which is found in the nature from hurricanes to seashells, was considered for flow field pattern of a PEMFC. Contrary to the bio-inspired designs proposed in previous studies, continuous smooth change in the flow direction through curved spiral channel and flow field geometry restrained to the rounded area was attained. Computational studies for the PEMFC performance with Fibonacci spiral flow channel were conducted by solving the governing electrochemical equations using the Ansys Fluent software. In addition to the Fibonacci spiral geometry, a novel rectangular spiral design and the conventional parallel design were also simulated for performance comparisons. Polarization, power density, and fuel cell power output per required compressor power curves were computed in addition to distribution contours of pressure, velocity, reactant concentrations, and water mass fractions for all three flow field designs. Fibonacci spiral design exhibited uniform reactant distribution, improved water management, and extremely low-pressure drop compared to the rectangular spiral and conventional parallel designs.

ACKNOWLEDGMENTS

TABLE OF CONTENTS

LIST OF FIGURES

LIST OF TABLES

1. INTRODUCTION

The depletion of fossil-based fuels and their negative environmental impacts force the energy sector to search for cleaner and more efficient energy sources and devices. Fuel cells, as one of the most promising alternative energy devices, are employed on a wide scale in many applications from automotive to portable electronic devices. Polymer electrolyte membrane fuel cells (PEMFC) are relatively superior to other types of fuel cells when their advantages are taken into account. Fast start up, low operation temperature, high power density, high reliability, and durability can be given as vital features expected from a power source. PEMFCs have been preferred to other types of fuel cells profoundly since these expectations are met better while releasing zero emissions to the environment.

Research carried out to improve PEMFCs performance has crucial importance. In addition to operating conditions and factors related fuel cell reaction kinetics and mass transport, PEMFC performance changes based on the design of its components, including membrane electrode assembly and bipolar plate. In this context, designing of flow channels manufactured over the bipolar plate has vital role on enhancement of fuel cell performance.

Numerical and experimental studies have been conducted to figure out the impact of flow field on performance of fuel cells. Uniform distribution of reactants is directly related to the flow field of a fuel cell. Uneven distributions of reactants result in local thermal stress at flow channels and poor water distribution within a fuel cell. Distribution of reactants has significant effects on not only the performance but also durability of PEMFCs [1, 2]. PEMFC is also exposed to energy losses caused by local flooding due to

poor removal of water. This problem can be reduced to a minimum level with proper flow field design of bipolar plate [3]. Designing flow field to acquire maximum PEM fuel cell performance is an optimization problem with multivariate. For this purpose, impact of numerous geometric parameters regarding bipolar plate flow field on the PEMFC performance should be studied to improve many other aspects, such reliability, durability and efficiency. Shape and cross section of the flow field, the ratio of channel width to rib width, channel depth ,creation of blockage with baffles in the flow field are used as variables of the optimization to enhance the performance of the fuel cell [4,5].

A versatile flow field was developed by Meenaksi et al. [6], creating a serpentine flow field with two inlets and outlets with four manifolds instead of one inlet and outlet with two manifolds that conventional designs have. Accordingly, different flow field characteristics such as interdigitated, serpentine, and counter flow could be obtained by changing actively used manifolds even though monotype flow channel was used. Polarization curve is the foremost guide that yields the overall performance of a PEMFC by showing the changes in current density with voltage changes. According to polarization curves obtained from the experiments conducted and current density distributions of different flow field designs mapped by an in-house measurement device, different flow field designs were compared with respect to their overall performances.

Another study on flow field design was conducted by Alrwashdeh et al. [7]. The impact of the small barriers applied to flow fields on the overall PEMFC performance was investigated based on the neutron radiographic method. Liquid water was accumulated and removed with a certain period behind and in front of the barrier without resulting in any local flooding or dehydration effect. Uniform water distribution and ideal membrane

proton conductivity took place compared to flow field without barrier. Additionally, another benefit of the applied barrier to flow field was that barriers and liquid water observed around the barriers drove the gas flow to the gas diffusion layer.

A hybrid flow channel geometry, which provides smooth transition from fully serpentine channel properties to interdigitated channel properties by changing the opening of the control valve linking the inlet channel to the outlet channel, was tested by Chen et al. [8] in order to determine optimum pressure difference between the inlet and outlet channels. The portion of the convective flow rate under the rib and pressure differences between inlet and outlet channels based on the magnitude of control valve opening were measured. They concluded that determination of optimum pressure difference between the inlet and outlet channels required to obtain maximum overall power output by utilizing the advantages of serpentine and interdigitated designs.

Heck [9] presented that pressure impact on the required auxiliary power and the reactant concentration supplied at the inlets could be reduced by providing reactants at the same pressure value. Reactants with the same inlet pressure were supplied at parallel and serpentine flow fields by applying backpressure to parallel flow field design in this study. Therefore, pressure effect on the power outputs of parallel and serpentine flow field was made equal. It was concluded that the performance difference between parallel and serpentine design was caused by the distribution effects alone. Kloess et al. [10] compared two flow field designs inspired from nature, a leaf design and a lung design, with conventional single serpentine and interdigitated designs with respect to overall power density output by taking into consideration pressure distribution and pressure drop using experimental and numerical methods. The velocities in both leaf and lung designs were

relatively small but more uniform due to much smaller pressure drop than that of conventional flow field design. Moreover, the best operation temperatures, humidity levels and backpressure values were reported for these two bio-inspired flow fields.

For all flow field configurations, observations clearly indicate that temperature increase improves the fuel cell performance based on the improved kinetics. However, after a certain temperature, it causes the membrane to dry. On the other hand, lower temperature might create water droplets rather than water vapor at the outlets. Therefore, special water management strategies could be required. In addition to the effect of the operation temperature, the PEMFC performance also increases with an increase in backpressure because more reactant is forced through the gas diffusion layer (GDL).

Arvay et al. [11] improved branching flow field configurations inspired from nature and investigated their performances relative to conventional serpentine and interdigitated designs by taking into account anode and cathode pressure drop, current density, and current density deviation values inside PEMFC. In addition, they presented that the flow configuration obeying the Murray law shows less current density deviation but higher pressure drop. Murray branching law explains mathematically relationship between the parent vessel's diameter and that of daughter channels found in human body [14].

Performance investigation of PEMFCs with different flow field configurations should be made at middle current density ranges since accuracy of commercial CFD software used at higher current density areas is somewhat low because of the formation of uncertain amount of liquid water that cannot be accounted for during the simulations [12].

A leaf flow pattern created by Roshandel et al. [12] showed better PEMFC performance compared to the conventional parallel and serpentine flow fields since this bio-inspired design showed more uniform distribution of oxygen concentration and less zero-velocity stagnation points inside the fuel cell.
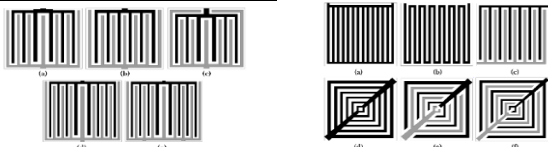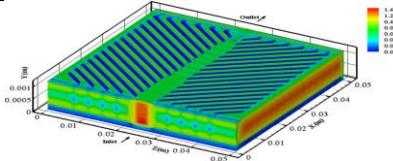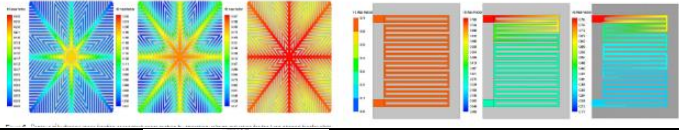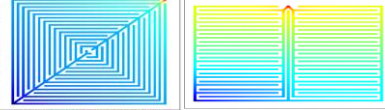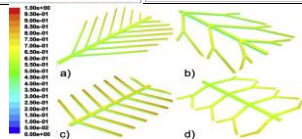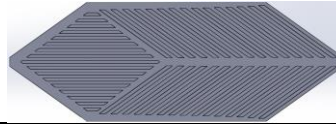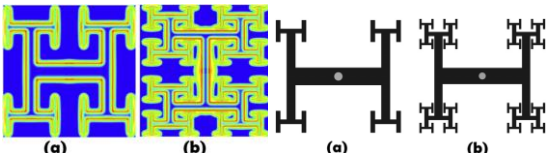
Flow resistance due to flow friction and pressure drop in different branching channels may not be equal. Flow tends to choose the path that has less flow resistance. This is because uniformities in terms of the reactant concentration distribution, velocity distribution, and pressure distribution take place. This, in turn, directly affects the fuel cell's overall performance. However, high pressure difference between inlet and outlet channels resulting from disconnection in interdigitated channels minimizes uneven distribution through convective flow. That is why interdigitated flow field designs generally exhibit the highest performance. However, auxiliary power requirement for the interdigitated flow field design is much higher compared to the other types of flow fields due to large amount of pressure drop. Guo et al. [13] have combined the advantages of conventional interdigitated flow channels with a bio-inspired leaf configuration obeying the Murray law. They noticed that oxygen concentration should be uniform throughout the flow channels. Thus, decrease in pressure and reactant concentration in flow channels from inlet to outlet can be compensated by changing the channel diameter from inlet to outlet, as seen in interdigitated bio-inspired design obeying the Murray law. In addition, use of the bio-inspired channel having bend with right angles should be avoided so as to prevent static points, formation of liquid water, and excess pressure and head loss [15]. Advantages of the same bio-inspired leaf configuration were further analyzed by Saripella et al. [16] by directly visualizing water distribution with this fuel cell.

An approach depending on entropy generation for performance comparison of tree-like flow configuration inspired from nature has been proposed by Damian-Ascencio [17]. Entropy generation analysis has been conducted with respect to thermal, fluid friction, and mass transport. They noted that entropy generation associated with thermal and fluid friction effects could be ignored, while the impact of entropy generation over uniformity of distribution of reactant gases caused by mass transport was emphasized.

Many different types of bio-inspired flow configurations for PEMFCs have been designed and their performances have been investigated. This is summarized in Table 1.1 below for convenience. When bio-inspired configurations considered by the previous research is taken into account, there does not exist a flow field having continuous smooth change in the flow direction instead of sudden changes with sharp bends, having symmetry in its configuration, having geometry restrained to rounded areas instead of corners, and having just parent channels without branching into daughter channels for avoiding flow resistance difference against flow because of different pressure drop seen in the different flow branching paths. A bio-inspired flow field configuration having all these characteristics has not been designed with its performance characteristics in the literature. Fulfilling these geometrical features, a well-known mathematical sequence found in the nature, from hurricanes to seashells, namely Fibonacci spiral, will be applied to the flow field pattern of a PEMFC in this thesis. The expectations from a fuel cell with proper flow field configuration are uniform reactant distribution, water management ability, high durability, low required compressor power input to overcome the pressure drop between inlet and outlet channels, high power output, and high power output per pumping power input. Polymer electrolyte membrane fuel cell with nature-inspired flow field design with

Fibonacci spiral geometry will be computationally investigated in this thesis for this unique

flow field configuration by comparing its performance with rectangular spiral design and

conventional parallel design.

Table 1.1. Bio-inspired flow field configurations in the literature

	Authors	Flow Field Configurations
1	Arvay et al. [11]	
2	Roshandel et al. [12]	
3	Guo et al. [13]	
4	Asadzade et al.[15]	
5	Kloess et al.[10]	
6	Damian-Ascencio et al.[17]	
7	Heck et al.[9]	
8	Ramos-Alvarado et al.[18]	

2.POLYMER ELECTROLYTE MEMBRANE FUEL CELLS (PEMFCs)

Conventional methods used to convert energy by burning fossil fuels release substantial amounts of harmful emissions to the environment. In addition to concerns for negative environmental effects, depletion of fossil fuel resources is another motivation in the search for cleaner and more efficient energy conversion devices. Fuel cells are considered as one of the most promising clean energy alternatives. In contrast to conventional energy systems that produce energy by burning fossil fuels, fuel cells have high performance efficiency because, unlike heat engines, fuel cells are not limited by the Carnot efficiency. The reason behind this fact is that chemical energy stored in the fuel in a combustion engine is converted to thermal energy through combustion and then heat is converted to mechanical energy through moving parts that is transformed to electrical energy, whereas chemical energy found in the fuel in a fuel cell is converted directly to electrical energy. If this difference is analyzed at the atomic scale, how a fuel cell converts chemical energy directly into electrical energy can be figured out. Burning of hydrogen fuel (H_2) takes place in an combustion engine as:

$$H_2 + \frac{1}{2}O_2 \rightleftharpoons H_2O \qquad (2.1)$$
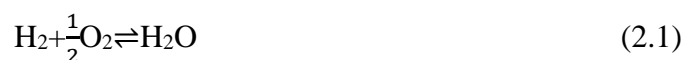
Hydrogen-hydrogen bond and oxygen-oxygen bond are broken and formed new hydrogen-oxygen bond between hydrogen and oxygen atoms and, as a result, water is produced. Due to the transfer of electron between atoms, breaking and forming of bonds take place in picoseconds [23]. Since bonding energy of the water product is lower than that of reactants,

the corresponding energy difference is emitted in the form of heat, which is then converted to mechanical energy followed by electrical energy. In contrast to the combustion engine, fuel cell working principle relies on utilizing electrons directly. Reactions take place spatially separated at anode and cathode sides of the electrolyte in a PEMFC as:

$$\text{Electrochemical reaction at anode side:} \quad H_2 \rightleftharpoons 2H^+ + 2e^- \qquad (2.2)$$

$$\text{Electrochemical reaction at cathode side:} \quad \frac{1}{2}O_2 + 2H^+ + 2e^- \rightleftharpoons H_2O \qquad (2.3)$$

$$\text{Overall reaction:} \quad H_2 + \frac{1}{2}O_2 \rightleftharpoons H_2O \qquad (2.4)$$
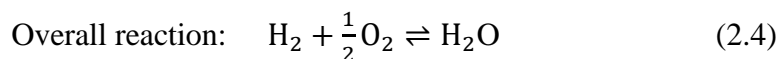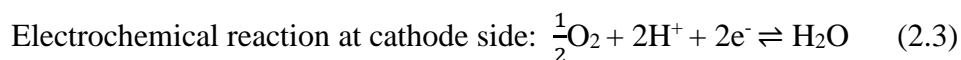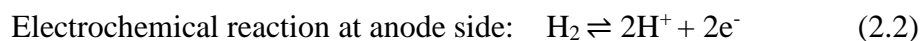
In Figure 2.1., electrochemical reactions are illustrated at nanoscale. An external circuit for electrons' flow is included in a fuel cell. Electrical current is obtained through an external circuit. Thereby, the time difference between breaking a bond and forming a bond is extended from an order of picoseconds.
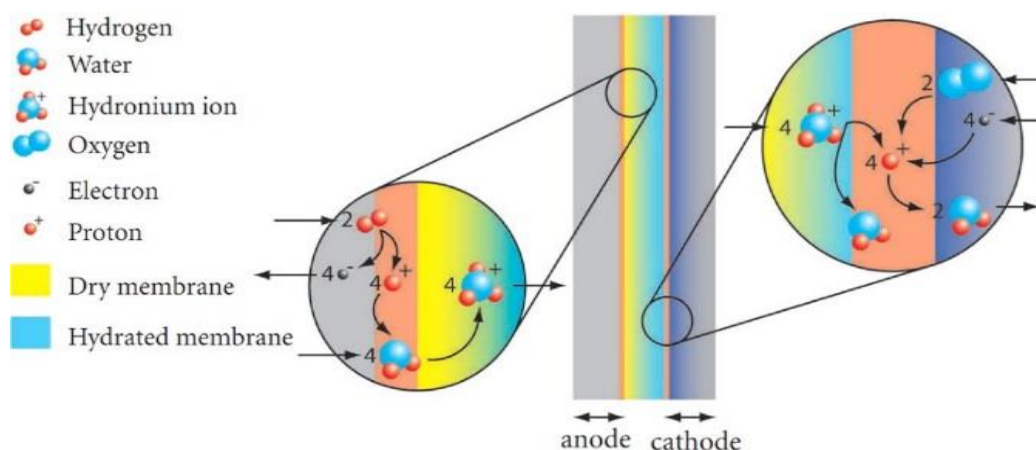
Figure 2.1. Chemical reactions taking place in a PEMFC [24]

Cross-section of a PEMFC is illustrated in Figure 2.2. Catalyst layers and gas diffusion layers consist of porous zones. In addition, solid ribs are placed between channels to enable electrons to transfer. Hydrogen gas is supplied to anode channel and then it reaches to anode catalyst layer through porous gas diffusion layer. Chemical reactions take place only at catalyst layers both on anode and cathode sides. At the anode catalyst layer, anode electrochemical reaction occurs following Equation 2.2.
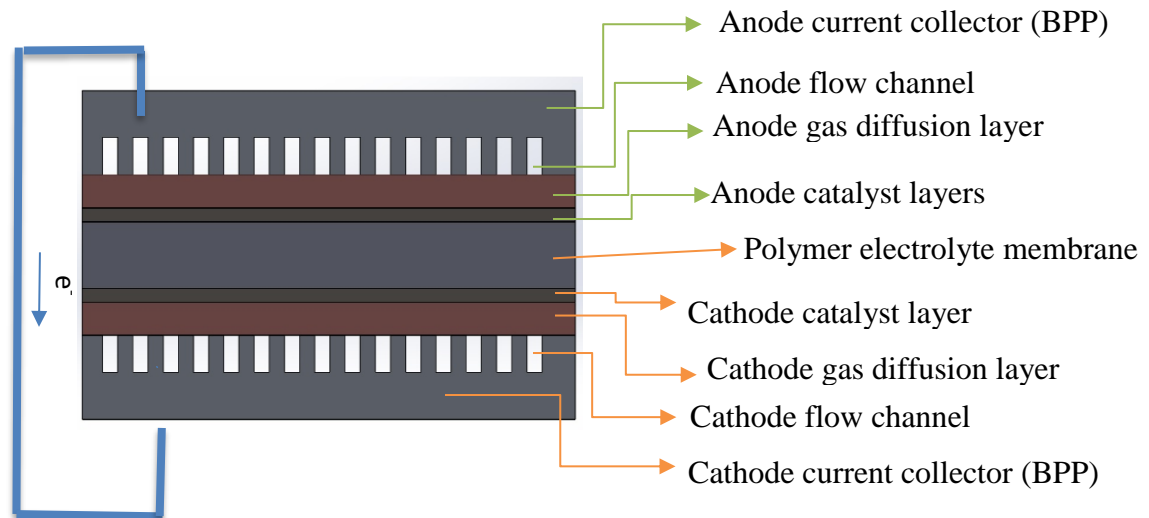
Figure 2.2. Cross-section of a PEMFC

Hydrogen ions and electrons are formed as a result of the anode half reaction. Electrons are transferred to cathode collector by using the solid parts of the anode gas diffusion layer, channel, and collector, respectively. After electrons enter the cathode collector, they reach cathode catalyst layer by using the solid parts of the cathode side. Hydrogen ions arrive at the cathode catalyst layer by means of diffusion through polymer membrane so as to combine with electron and oxygen.

Then, cathode half-reaction occurs at cathode catalyst layer as noted in Equation 2.3. Water is created only as a product of hydrogen fuel which means that PEMFC releases zero emission to the environment.

2.1 ELECTROCHEMICAL ENERGY CALCULATIONS OF PEMFC

PEMFC is an electrochemical device. Chemical energy included in reactants is converted to electrical energy as indicated in Equation 2.5. *G, U, T, H, $W_{electric}$, P,* and *V* are Gibbs free energy, internal energy, temperature, enthalpy, maximum electrical work, pressure, and volume, respectively.

$$G=H\text{-}TS; \quad H=U+PV \tag{2.5a}$$

$$dG = dU\text{-}Tds\text{-}SdT+PdV+VdP \tag{2.5b}$$

$$dU=TdS\text{-}(PdV+dW_{electric}) \tag{2.5c}$$

$$-\Delta G = W_{electric} \tag{2.5d}$$

Equation 2.5d indicates that maximum electrical energy that can be obtained from a fuel cell equals the Gibbs free energy difference as long as chemical reactions occur at constant temperature and pressure. At standard temperature and pressure (STP) (25 °C, 1 atm), maximum potential reversible voltage *(E^0)* for PEMFC can be calculated by using Equation 2.6.

$$E^0 = \frac{-\Delta G}{nF} = \frac{-237170 \; J/mol}{2mol \; e*96485C/mol} = 1.229 \; V \tag{2.6}$$

In Equation 2.6, *F* and *n* represent the Faraday constant (96485C/mol) and number of moles of electrons transferred corresponding per mole of fuel, respectively. In this calculation, Gibbs free energy is found by taking the overall reaction (Equation 2.1) of the fuel cell into account. Equation 2.6 cannot be used for energy calculation of a PEMFC that operates under non-standard conditions such as the typical operating conditions at 80 °C and 2-3 atm. In this case, reversible ideal PEMFC voltage is calculated by using the Nerst equation given in Equation 2.7.

$$E = E^0 + \frac{\Delta S}{nF}(T - T^0) + \frac{RT}{nF}In(\frac{1}{\sqrt{P_{O2}} \ P_{H2}}) \qquad (2.7)$$

Here, E^o is the ideal reversible voltage under STP conditions, P_{o2}, P_{H2} are the partial pressures of oxygen and hydrogen gases at anode and cathode inlets, *R* is the universal gas constant, *T* is the operation temperature, and T^0 is the standard temperature. The actual fuel cell voltage will be less that this ideal voltage calculated from the Nerst equation because of three main losses that occur, namely activation losses (η_{act}), ohmic losses (η_{ohmic}), and concentration losses ($\eta_{concent.}$). Reactants at the anode and cathode side must exceed activation energy for the electrochemical reactions to commence. The voltage compensation for reactions kinetics at low currents is called activation losses. Fuel type, working temperature and electrolyte type have strong effects on reaction kinetics. During ionic and electronic conduction at the electrolyte and the external circuit, ohmic losses become important at medium currents due to the encountered resistance to hydrogen ion charge transport. Ohmic losses *(η_{ohmic})* due to electronic conduction are much less than ohmic losses due to ionic conduction in the membrane [23]. High ionic conductivity, low electronic conductivity, and low fuel crossover are fundamental expectations from the ideal

electrolyte. Mass transport inside the PEMFC is another important factor that should be paid attention at high currents. Effective delivery of reactants gases of H_2 and O_2 to anode and cathode side and removal of water produced from cathode side play crucial roles for reducing mass transport losses to a minimum level. Consequently, the actual voltage obtained from a PEMFC is calculated by accounting for activation losses (η_{act}), ohmic losses (η_{ohmic}), and concentration losses $(\eta_{concent.})$ as

$$V=E- \eta_{ohmic} - \eta_{act} - \eta_{concent.} \tag{2.8}$$

Polarization curve gives the overall performance of a fuel cell from the relationship between current density (A) and fuel cell voltage (V) shown in Figure 2.3.
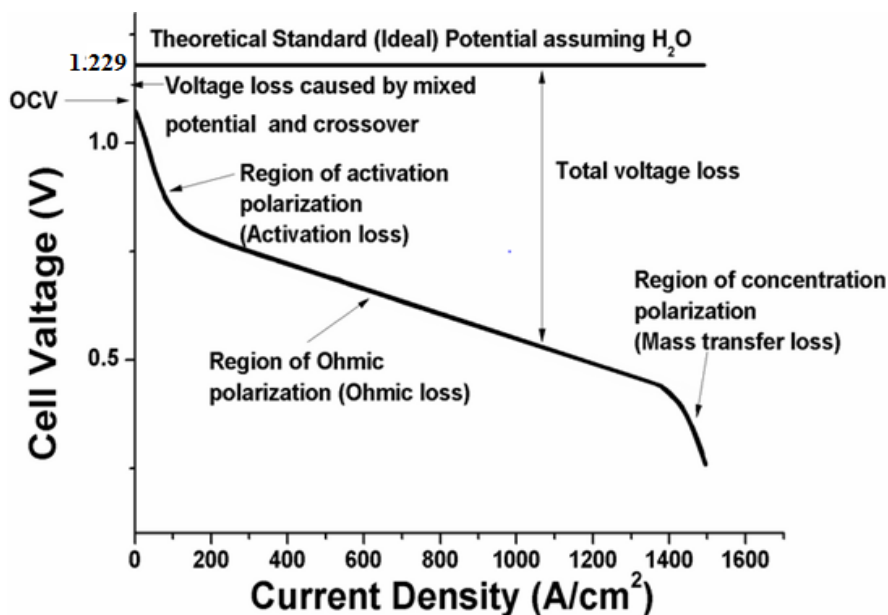
Figure 2.3. Fuel cell polarization curve

Ideal thermal efficiency of a PEMFC can be calculated from the Gibbs free energy and the enthalpy of water:

$$\epsilon_{thermo} = \frac{\Delta G}{DH_{H2O}} = \frac{-237.17}{-286} = 0.83 = 83\% \tag{2.9}$$

In addition, voltage losses discussed above cause total efficiency to decrease as

$$\epsilon_{voltage} = \frac{real\ voltage\ (V)}{reversible\ voltage\ (E)} \tag{2.10}$$

Moreover, some differences between utilized hydrogen fuel corresponding to generated electricity and the total amount of hydrogen fuel supplied to a fuel cell can be seen.

$$n_{H2} = \frac{i}{n*F} = \frac{i}{2*96400} \tag{2.11}$$

$$\epsilon_{fuel} = \frac{n_{H2}}{n_{H2total}} = \frac{1}{\lambda} \tag{2.12}$$

where $n_{H2total}$ and λ are the total fuel supplied to fuel cell and stoichiometric factor, respectively. Total PEMFC cell efficiency (ϵ_{total}) can then be expressed by

$$\epsilon_{total} = \epsilon_{thermo} * \epsilon_{voltage} * \epsilon_{fuel} \tag{2.13}$$

2.2. 3D MATHEMATICAL MODELING OF PEMFC

The three-dimensional fluid flow was analyzed by harnessing the Navier-Stokes transport equation:

$$\frac{\partial}{\partial t} \int_V \rho\phi\ dV + \oint_A \rho\phi V \cdot dA = \oint_A \Gamma_\phi \nabla\phi \cdot dA + \int_V S_\phi\ dV \tag{2.14}$$

Here, ϕ is the mass moving, t is the time, A is the superficial area, V is the volume, Γ_ϕ is moved quantity via diffusivity, and S_ϕ is the source term associated with ϕ. The first term in the equation represents the transient transport of ϕ, the second term is the transport of ϕ by convection, the third term is related to the transport of ϕ by diffusion, and the fourth term represents the source of ϕ [11]. Governing equations (see Table 2.1) associated with the electrochemical and fluid dynamics [12,17,25,26] were solved using the ANSYS Fluent software in order to model a PEMFC.

Table 2.1. Governing equations of PEMFC model

Governing equations	Mathematical expression	Source terms
Conservative of mass (continuity)	$\vec{\nabla}. \ (p\,\vec{u}) = S_m$	$S_m{=}S_{H_2}{+}S_{H2O,\,a}$ $S_m{=}\ S_{O_2}{+}S_{H2O,\,c}$
Momentum equation	$(\vec{u}.\vec{\nabla}).p\vec{u} = -\,\vec{\nabla}P + \vec{\nabla}(\mu\vec{\nabla}.\vec{u}) + S_p$	$S_p = -\ (\frac{\mu\,\vec{u}}{K})$
Transport of species	$(\vec{u}.\vec{\nabla}).p\ Y_i = \vec{\nabla}\ \vec{J_i} + S_i$	$S_{H_2} = -\frac{M_{w,H_2}}{2F}\,R_{an}$ $S_{H_2O,a} = -\frac{M_{w,H_2O}}{F}\,R_{an}$ $S_{O_2} = -\frac{M_{w,O_2}}{4F}\,R_{cath}$ $S_{H_2O,c} = \frac{M_{w,H_2O}}{2F}\,R_{cath}$

Electron completes its flow by using solid conductive material while ionic (protonic) flow occurs through the membrane electrode assembly (MEA). Equation 2.15 was used to compute solid phase electric potential because of electron transport at solid parts of the current collectors, the gas diffusion layers, and the catalyst layer. Equation 2.16

explains the electric potential caused by proton ion transport at the polymer electrolyte membrane and catalyst layer. The difference between phase potential of solid and phase potential of membrane plays a crucial role to initiate the electrochemical reactions at catalyst layers.

$$\nabla \cdot (\sigma_{sol} \nabla \varphi_{sol}) + R_{sol} = 0 \tag{2.15}$$

$$\nabla \cdot (\sigma_{mem} \nabla \varphi_{mem}) + R_{mem} = 0 \tag{2.16}$$

In the above equations, σ is the electric conductivity, φ is the electrical potential, and R is the volumetric transfer current. Transfer current values in the solid phase and in the membrane phase are given depending on transfer current on the anode and cathode catalyst layers as

$$R_{sol} = \text{-}R_{an} = R_{cat} \ ; \ \ R_{mem} = R_{an} = \text{-} \ R_{cat} \tag{2.17}$$

The boundary conditions to determine φ_{sol} and φ_{mem} at anode boundary and cathode boundary were:

At anode boundary: $\qquad \dfrac{\partial \varphi_{mem}}{\partial n} = 0 \tag{2.18}$

$$\dfrac{\partial sol}{\partial n} = 0 \tag{2.19}$$

At cathode boundary: $\qquad \dfrac{\partial \varphi_{mem}}{\partial n} = 0 \tag{2.20}$

$$\varphi_{sol} = V_{cell} \tag{2.21}$$

Butler–Volmer equation (Equation 2.22) was used to find transfer currents afterwards to solve the source terms in Equation 2.23.

$$R_{an} = i_{ref}^{an} \left(\frac{[H_2]}{[H_2]_{ref}} \right)^{\gamma_{an}} (e^{\frac{\alpha_{an}F\eta_{an}}{RT}} - e^{\frac{-\alpha_{cat}F\eta_{an}}{RT}}) \tag{2.22a}$$

$$R_{cat} = i_{ref}^{cat} \left(\frac{[O_2]}{[O_2]_{ref}} \right)^{\gamma_{cat}} (e^{\frac{\alpha_{an}F\eta_{cat}}{RT}} + e^{\frac{-\alpha_{cat}F\eta_{cat}}{RT}}) \tag{2.22b}$$

Here, i_{ref}^{an} and i_{ref}^{cat} are the reference exchange current densities, γ_{cat} and γ_{an} the concentration coefficients for the anode and cathode sides, α_{an} and α_{cat} the water transfer coefficient for anode and cathode sides, η_{an} and η_{cat} the surface over potential at anode and cathode sides, and $[H_2]_{ref}$ and $[O_2]_{ref}$ the reference concentrations of H_2 and O_2. Source terms for the chemical species were calculated from

$$S_{H_2} = -\frac{M_{w,H_2}}{2F} R_{anode} \tag{2.23a}$$

$$S_{O_2} = -\frac{M_{w,O_2}}{4F} R_{cathode} \tag{2.23b}$$

$$S_{H_2O} = -\frac{M_{w,H_2O}}{2F} R_{cathode} \tag{2.23c}$$

Additional transport equations for water liquid saturation and water content should be taken into account for modeling the two-phase flow. The saturation model approach was used for the liquid water formation and transport from Equation 2.24 for the calculation of water saturation.

$$\frac{\partial(\epsilon \rho_l s)}{\partial t} + \nabla \cdot \left(\rho_l \vec{V}_l s\right) = r_w \tag{2.24}$$

Here, the subscript l stands for liquid water, $\vec{V}_l$ is the velocity vector, s is water saturation, and r_w is the condensation rate. Inside the porous zones, the capillary diffusion term must change with the convective term in the above equation, as given by Equation 2.25, in order to account for transport phenomena inside GDL, where capillary forces have the main effect on the transport of liquid water.

$$\frac{\partial(\epsilon \rho_l s)}{\partial t} + \nabla \cdot \left(\rho_l \frac{Ks^3}{\mu_l} \frac{dp_c}{ds} \nabla s\right) = r_w \tag{2.25}$$

Here, K is the permeability and p_c is the capillary pressure, which can be calculated from:

$$P_c = \begin{cases} \dfrac{\sigma cos\theta c}{\frac{K^{0.5}}{\varepsilon}} (1.417(1-s) - 2.12(1-s)^2 + 1.263(1-s)^3) & \theta c < 90^0 \\[2em] \dfrac{\sigma cos\theta c}{\frac{K^{0.5}}{\varepsilon}} (1.417s - 2.12s^2 + 1.263s^3) & \theta c > 90^0 \end{cases} \qquad (2.26)$$

where σ is the surface tension (N/m) and θc is the contact angle. Species diffusivities in the gas phase were computed from:

$$D_i = \epsilon^{1.5}(1-s)^{r_s} D_i^{ref} \left(\frac{p_{ref}}{p}\right) \left(\frac{T_{ref}}{T}\right)^{1.5} \qquad (2.27)$$

$$\vec{J_i} = -\,p\,D_i\,\vec{\nabla}.Y_i$$

ϵ is the porosity, r_s is the pore blockage exponent, and, D_i^{ref} is the mass diffusivity of species at the reference pressure and temperature. Other parameters in Equation 2.27 are: $P_{ref} = 101325$ N/m^2, $T_{ref} = 300K$, and $r_s = 2.5$. Clogging effect observed in porous zones was taken into account by multiplying the diffusivity term by $(1-s)^{r_s}$.

Table 2.2. Parameters used in Ansys during PEMFC simulations

Model Parameter	Units	
Ref. Current Density-Anode	A/m^3	4.48×10^5 [13]
Ref. Current Density-Cathode	A/m^3	4.48[13]
Catalyst layer Surface to Volume ratio	m^{-1}	1.25×10^7[13]
Ref. Concentration-Anode	kmol/m^3	1.0
Ref. Concentration -Cathode	kmol/m^3	1.0
Concentration Exponent -Anode	-	0.5[27]
Concentration Exponent -Cathode	-	1.0[27]
Exchange Coefficient-Anode	-	1.0[13]
Exchange Coefficient-Cathode	-	1.0[13]
Open Circuit Voltage	Volt	1.0
Leakage Current	A	0.0
Reference Difusivity-H$_2$	m^2/s	8×10^{-5}[13]
Reference Difusivity-O2	m^2/s	2×10^{-5}[13]
Reference Difusivity-H$_2$O	m^2/s	5×10^{-5}[13]
Saturation Exponent (Pore Blockage)	-	2.0[27]

Ohmic losses due to ionic and electronic transport in the PEMFC reduce the fuel cell power output. Resistance effect in the membrane against ionic transport is more dominated than resistance force against the electronic flow. Therefore, ohmic losses based on membrane ionic conductivity, σ_{mem} and membrane thickness δ_{mem} are presented as

$$\eta ohm = \frac{\delta mem}{\sigma mem} \tag{2.28}$$

Membrane ionic conductivity was computed from Equation 2.29 depending on the water content, λ:

$$\sigma_{mem} = (0.514\ \lambda - 0.326)\ exp(1268\ (\frac{1}{303} - \frac{1}{T}) \tag{2.29}$$

The water content λ can be calculated from:

$$\lambda = \begin{cases} 0.043 + 17.18a - 39.85a^2 + 36a^3 & a < 1 \\ 14 + 1.4(a-1) & a > 1 \end{cases} \tag{2.30}$$

where a is water activity expressed as

$$a = \frac{X_{H2O}\ P}{P_{sat}} \tag{2.31}$$

In the above equation, P_{sat} is the saturation pressure inside the membrane, X_{H2O} is the water vapor molar fraction, and P is the local pressure. Saturation pressure, P_{sat}, can be estimated from the following curve fit to water saturation properties:

$$log_{10}P_{sat} = -2.1794 + 0.02953(T-273.17) - 9.1837\ 10^{-5}(T-273.17)^2$$

$$+ 1.4454\ 10^{-7}\ (T-273.17)^3 \tag{2.32}$$

Therefore, mass continuity, momentum in (x, y, z) directions, energy, chemical species (H_2, O_2, H_2O), solid phase potential, membrane phase potential, liquid saturation, and water content were solved for 3D fluid flow phenomena in a PEM fuel cell in the present computational study.

3. FLOW FIELD DESIGN INSPIRED FROM NATURE

Engineering has long been inspired by the nature. The existing natural systems are generally considered nearly ideal because they have been evolving for survival for very long time scales. Because these systems observed in the nature are the most efficient in their segments, bio-inspired solutions have been employed to various engineering problems faced in real life.

As discussed above in the introduction part, several PEM fuel cell designs with bio-inspired flow configurations have recently been suggested. While nature-inspired flow channels with angular flow patterns have been designed and investigated, spiral curved flow geometry has not been considered up to now. For this reason, one of the well-known mathematical ratio found in nature, namely golden ratio, will be implemented in the present study in order to design of flow channels of a PEM fuel cell and investigate its performance.

Golden ratio, which is an irrational number corresponding to 1.6180339, is a special number like pi constant *(π),* which is the ratio of a circle's circumference to its diameter. Golden ratio is obtained after one quantity is divided into two integral. If the ratio of the larger integral to the other small integral equals the ratio of the sum of the two integrals to the larger integral, it is called the Golden ratio and equals to 1.6180339. Golden ratio, larger quantity, and other small quantity are represented by *φ, x*, and *y* respectively.

$$\varphi = \frac{x+y}{x} = \frac{x}{y} = \frac{1+\sqrt{5}}{2} = 1.6180339 \tag{3.1}$$

In addition, ancient Greeks and Egyptians are the first known societies that have used the golden ratio in their art and architecture with just aesthetic concern. Phidias is the first known artist who used golden ratio for design of his sculpture in 500 BC [28].

3.1   DESIGN OF PEM FUEL CELL BIPOLAR PLATE CHANNELS BASED ON   FIBONACCI SPIRAL

Around 1200`s, Leonardo Fibonacci discovered the relationship between golden ratio and Fibonacci sequences created by himself. A number in Fibonacci series is addressed by sum of the two preceding numbers [29].
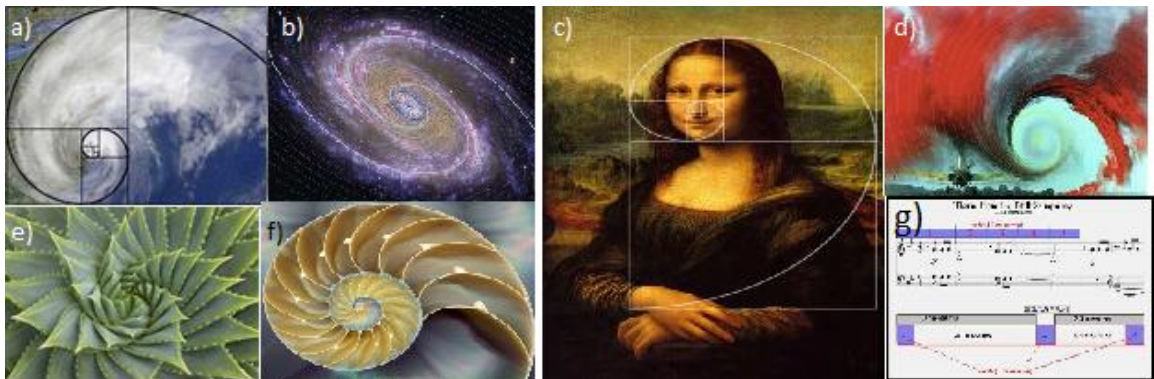

Figure 3.1. Some examples of Fibonacci number found in nature and art a) hurricane, b) cosmos, c) portrait made by Leonardo da Vinci, d) phi vortex, e) aloe plant leaves, f) sea shells, g) fifth symphony composed by Beethoven

The expression for the Fibonacci sequence can be written as

$$X_n = X_{n-1} + X_{n-2} \tag{3.2}$$

The Fibonacci sequence starts with 1 and 1, goes 1, 1, 2, 3, 5, 8, 13, 21, 34, 55, 89…The ratio between the consecutive numbers found in the Fibonacci sequences progressively approaches the golden ratio value. Some examples of Fibonacci spiral observed in the nature, art, and architecture are given in Figure 3.1. Leonardo da Vinci created paintings and drawings using the Fibonacci spiral ratio. Arrangements of some plant leaves also exhibit Fibonacci spiral configuration. When the hurricanes are geometrically analyzed, Fibonacci series remarkably are noticed in their shapes. In Milky Way, there exist three types of galaxies; spiral, elliptical, and irregular. Dust, stars and gas rotate around the same center in the same direction, forming Fibonacci spiral shapes in the spiral types of galaxies. Airfoils create phi vortex that has the form of Fibonacci spiral, similar to seashells. Fibonacci spiral configuration is either forced to obey instinctively by nature, as seen in galaxies, seashells, hurricanes, and aloe plant leaves or implied by artists for their arts, as seen in the portraits made by Leonardo da Vinci and fifth symphony composed by Beethoven. Samples found in nature or art influenced by Fibonacci spiral configuration somehow have distinguishable advantages. In engineering, Hsu et al. [21] have made performance investigation and optimization by designing a heat exchanger obeying Fibonacci sequence. Benovali et al. [22] have utilized Fibonacci sequence for control systems. In addition to these two studies, there are many engineering applications utilizing Fibonacci sequence. Based on the above examples utilizing Fibonacci sequence throughout the history, Fibonacci spiral configuration will be applied to the flow field channels of PEMFC possibly for the first time in this thesis. Polymer electrolyte membrane fuel cell with nature-inspired flow field design with this unique flow field configuration will be

evaluated and its performance will be compared to rectangular spiral design and conventional parallel design.

3.2. COMPUTATIONAL METHODS

3.2.1 Mesh and Model Settings. Ansys Fluent 18.0 Fuel Cell Add-on module was utilized in order to solve the complex governing equations and to make performance comparisons among PEMFCs with different flow field patterns. Same software was used by Guo et al. [13] and Saripella et al. [16] for performance comparisons among their PEMFCs with different flow channels. They validated their simulation results with experimental studies. The same model parameters, which are given in Section 2.2 in Table 2.2, were also used in this thesis. Fibonacci spiral design, rectangular spiral design, and conventional parallel design given in Figure 3.2 were geometrically created and computationally studied.

Rectangular spiral design and parallel design have rectangular active areas while Fibonacci spiral design has round active area. Geometric design parameters are presented in Table 3.1. Ansys Workbench 18.0 was used to create structural mesh with 1.6 million hexahedral cells. Maximum element size for mesh was 0.25 mm. Parallel design, rectangular spiral design, and Fibonacci spiral design have orthogonal qualities of 0.99,1 and 0.6, respectively. Orthogonal quality is an indication of mesh quality. Orthogonal quality has value between 0 and 1, where values close to 0 mean lower qualities. If the orthogonal quality values are smaller than 0.1 or 0.2, the mesh quality must be improved. Therefore, orthogonal quality of 0.6 is accepted as sufficient. Channel layers and bipolar

plate layers have 5 cells across, while gas diffusion layers, catalyst layers, membrane layer have 4 cells across as, demonstrated in Figure 3.3. Moreover, as shown in Figure 3.4, there are past studies in the literature that have different flow fields designs with similar flow inlets and outlets to the present Fibonacci spiral design.

During the simulations, heat caused by electrochemical reaction, current transport inside the catalyst layer, water transport through membrane, ohmic heating, and electrochemistry sources were taken into account in addition to governing equations of mass, energy, and momentum [19].
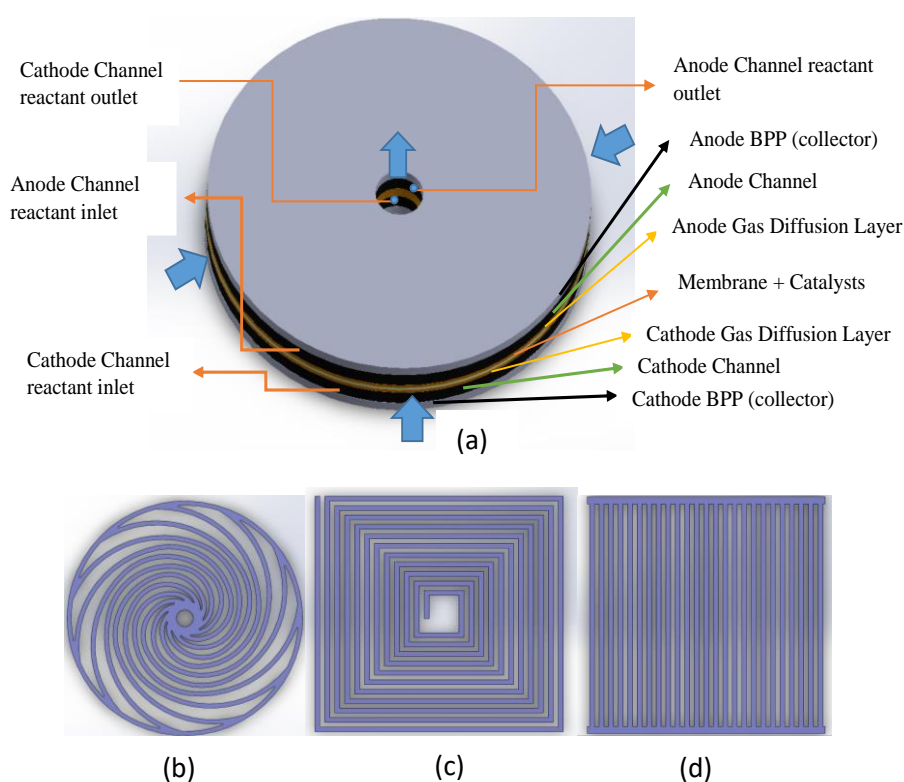

Figure 3.2. Illustration of different flow geometries (a) General illustration of fuel cell with round geometry, (b) Fibonacci spiral flow channel, (c) Rectangular spiral channel, (d) Conventional parallel channel

Computed velocities from mass conservation equation were used to calculate pressure values by using the SIMPLE algorithm, which computes the pressure correction value based on face flux computed from momentum equation with initial pressure value and from the mass conservation equation [19].Then, species transport equations were solved with the corrected parameters. Solid phase and membrane phase potentials were also solved with iterations until convergence [17]. Solution method for gradient was set as the least square cell-based, standard was set for pressure, second-order upwind was set for density, momentum, species, water saturation, energy, electric potential, protonic potential, and water content. Anode and cathode inlet had mass flow inlet boundary condition while anode and cathode outlet had pressure outlet boundary condition. Mass flow rates for inlet conditions were calculated by using the conditions given in Table 3.2.

Table 3.1. Geometric design parameters of fuel cell with parallel, rounded
Fibonacci spiral, and rectangular spiral configuration channel

Geometric Parameter	Value
Total active area	25 cm^2
Parallel design - Channel area/total active area	53%
Rounded Fibonacci Spiral design - Channel area/total active area	44%
Rectangular Spiral design - Channel area/total active area	48%
Total bipolar plate (BPP) thickness	2.5 mm
Channel depth	1.5 mm
Channel width	1 mm
Rib width for parallel and rectangular spiral	1 mm
Gas diffusion layer (GDL) thickness	0.35 mm
Catalyst layer thickness	0.01 mm
Electrolyte membrane thickness	0.15 mm
Total PEMFC cell thickness	5.87 mm

3.2.2 Approach to Case Runs during Simulations. Constant voltage values were set for cathode solid phase potential from 0.25 V to 0.85 V with 0.1 V increments. Current density corresponding to a fixed voltage value was calculated for each flow field configuration to create polarization and power density curves. Zero backpressure was set for all flow designs. However, inlet pressure must be different depending on the flow design because of the differences in pressure drops. Pressure drop was negligible for Fibonacci spiral and parallel designs while it was much higher for the rectangular spiral design. Reactants must be supplied with a pressure to overcome the pressure drop. Therefore, reactants must be supplied with a gage pressure of 34,000 Pa to the cathode side and with a gage pressure of 3300 Pa to the anode channel in the rectangular spiral design. In each fuel cell design, flow paths had lengths of 56 mm, 100 mm, and 1275 mm for Fibonacci spiral, conventional parallel, and rectangular spiral designs, respectively. These pressure drop values computed by the software were validated with hand calculations by substituting initial condition and length of flow paths mentioned above. Anode and cathode inlet pressure factors for rectangular spiral design must be taken into consideration so as to calculate mass flow rate in addition to the operating conditions given Table 3.2.

Table 3.2. Operating conditions for calculations of inlet mass flow rates

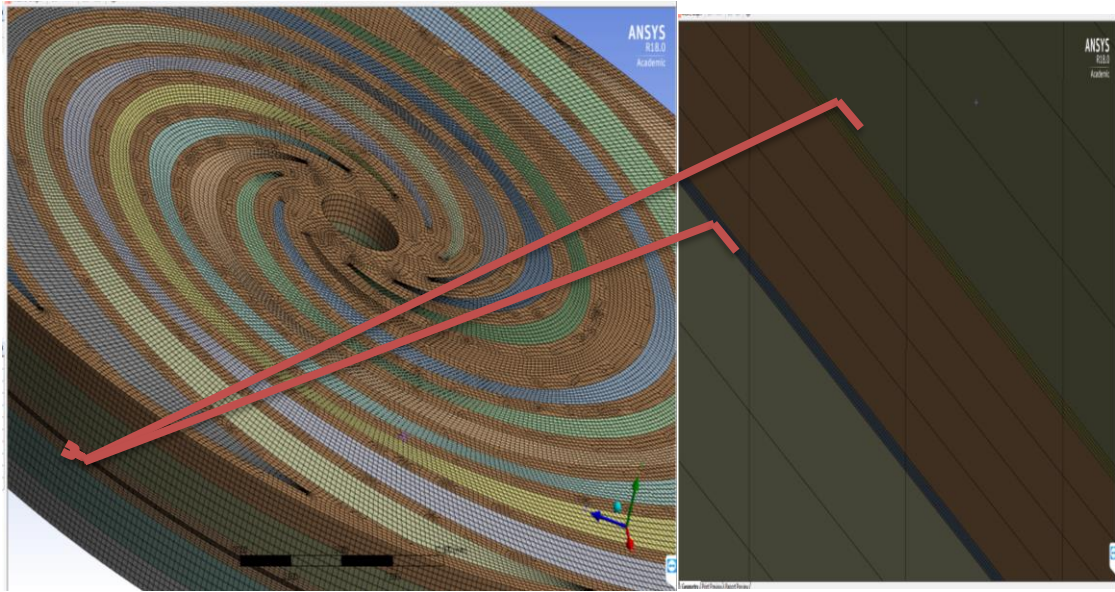| Operating conditions in the simulations	Values
Reactant stoichiometry at anode inlet	2
Reactant stoichiometry at cathode inlet	2
Temperature at inlets and boundaries	348 K
Gage pressure at anode and cathode outlet	0 Pa
Relative humidity at anode inlet	100%
Relative humidity at cathode inlet	75%
Current density	2 A/cm^2

Figure 3.3. Illustration of created grid (a) Mesh illustration of layers (b) Demonstration of catalyst layer and membrane mesh layer in detail

Convergence check was accomplished in three steps. First step was to check residual display as change in residual was monitored as long as the related equations were solved. Constant decline should be seen in residual values for convergence [20]. Second criteria for convergence was that the current density values at the anode terminal, cathode terminal, and interior electrolyte interface must be converged with current density values generated corresponding to consumption of species at anode and cathode sides. Obtained current density value depending on species consumption was given in Equation 2.23 in Section 2.2. The third criteria to decide whether or not convergence was achieved so that obtained solutions were reliable was that current density values should not change with further iterations.

Table 3.3. Inlet operation conditions at anode and cathode side for each flow design

| Operation Condition	Units	Values
Rectangular Spiral		
Cathode Inlet pressure	Pa, gage	34000
Anode Inlet Pressure	Pa, gage	3300
Mass flow rate Cathode Inlet	kg/s	4.15e-05
Oxygen mole fraction at cathode Inlet		0.165
Water vapor mole fraction at cathode Inlet		0.210
Mass flow rate at anode inlet	kg/s	6.36e-06
Hydrogen mole fraction at anode inlet		0.637
Water mole fraction at anode inlet		0.362
Parallel design and Rounded Fibonacci Spiral Design		
Cathode Inlet pressure	Pa, gage	0
Anode Inlet Pressure	Pa, gage	0
Mass flow rate Cathode Inlet	kg/s	4.43e-05
Oxygen mole fraction at cathode Inlet		0.150
Water vapor mole fraction at cathode Inlet		0.281
Mass flow rate at anode inlet	kg/s	6.65e-06
Hydrogen mole fraction at anode inlet		0.625
Water mole fraction at anode inlet		0.375
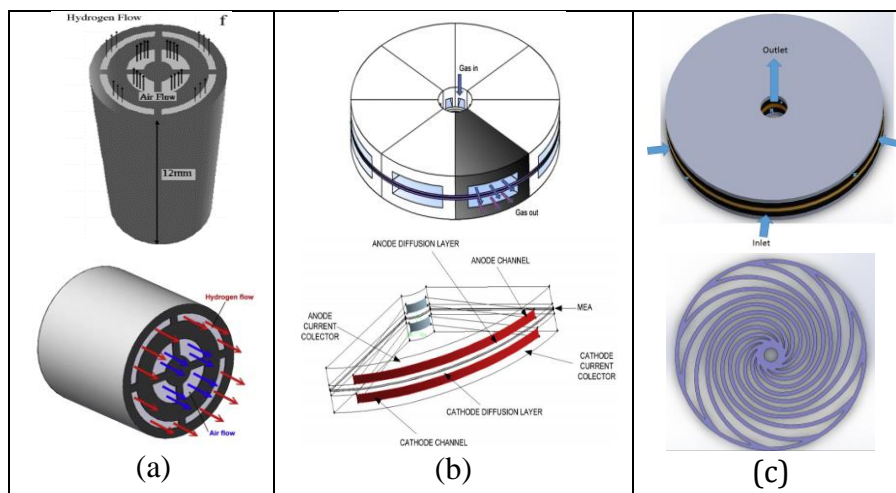
Figure 3.4. Different fuel cell designs having similar flow inlet and
outlet trend with Fibonacci spiral design a) annular PEMFC [32],
b) radial PEMFC [25], c) Fibonacci spiral PEMFC

3.3 RESULTS AND DISCUSSION

As seen in power density curves in Figure 3.5, all three flow field configurations generated their maximum power density values at around a voltage of 0.45 V. As a result, a voltage value of 0.45 was chosen for performance comparisons among different flow field configurations.
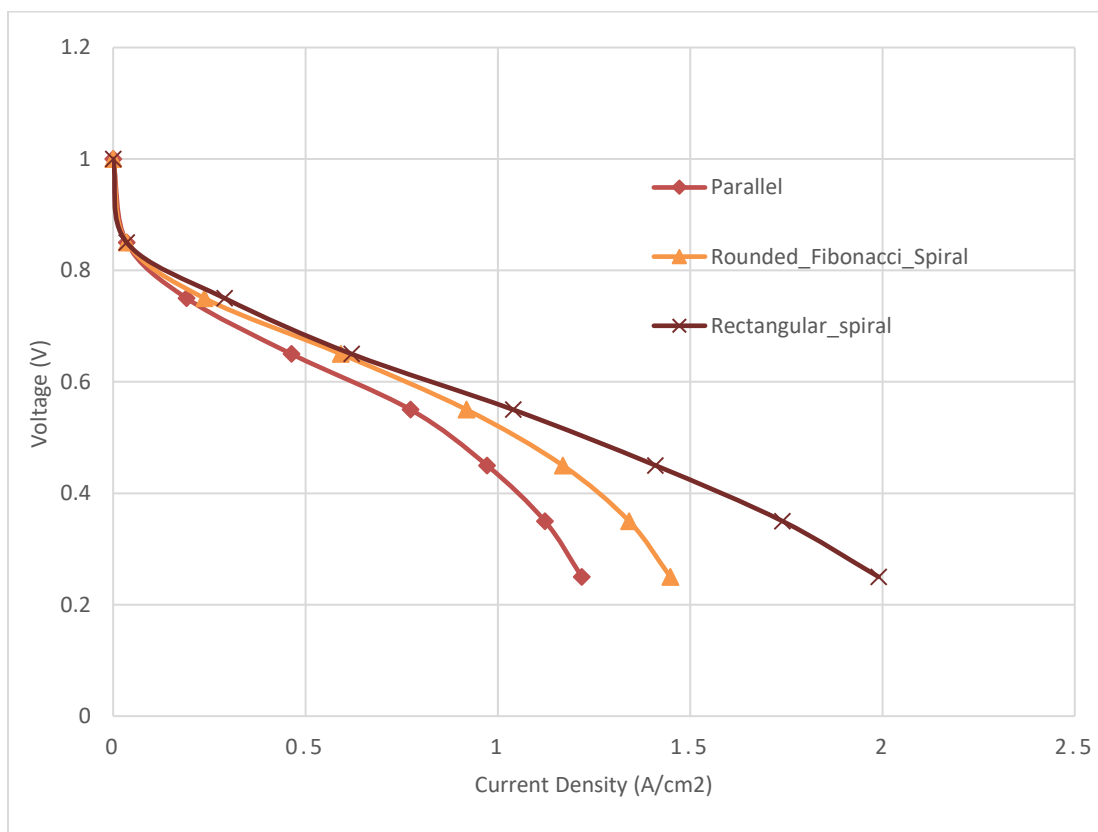
(a) Polarization curves

Figure 3.5. Performance comparisons of parallel, rounded Fibonacci spiral, and rectangular spiral (a) polarization curves (b) power density curves
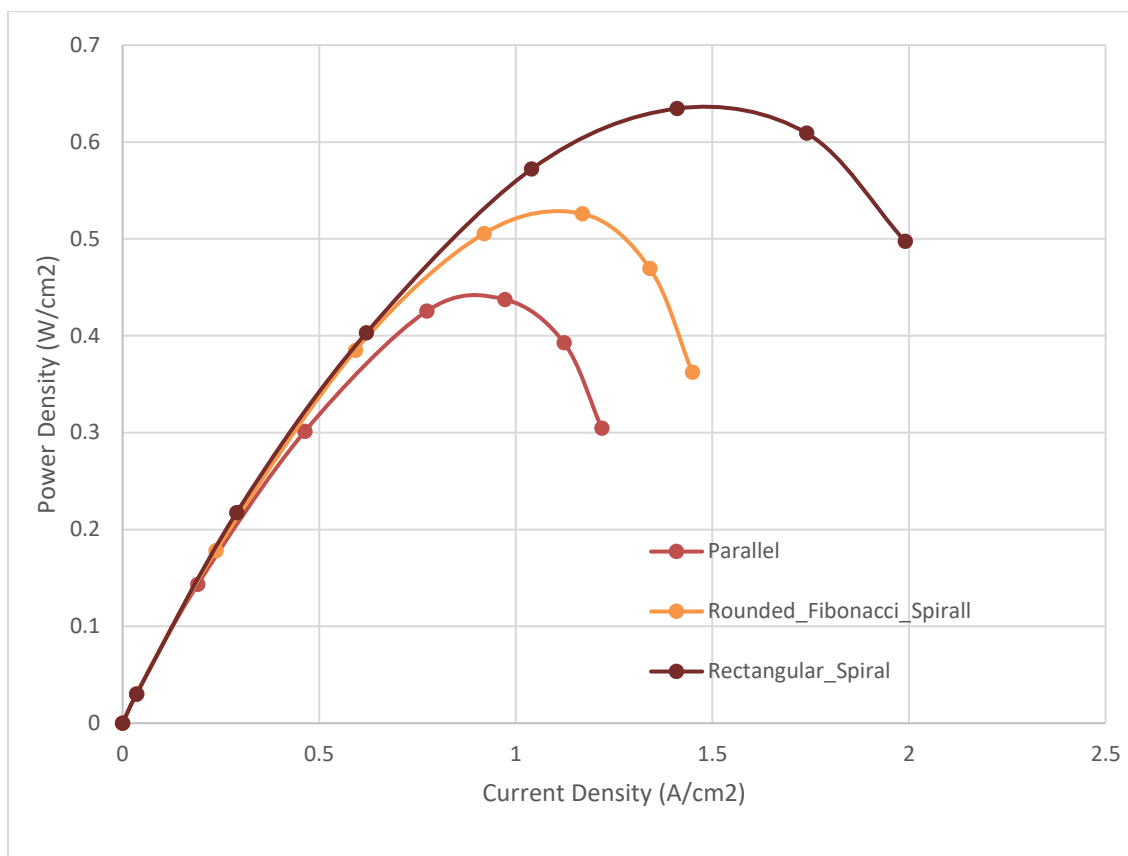
(b) Power density curves

Figure 3.5. Performance comparisons of parallel, rounded Fibonacci spiral,
and rectangular spiral (a) polarization curves (b) power density curves (cont.)

Variation in current density with voltage given in polarization curves yielded general fuel cell performance. However, detailed performance evaluations were also made by looking at current density distributions at gas diffusion layer (electrode). Current density distributions given in Figure 3.6 exhibited to what extent chemical reactions occurred at different parts of the active reaction area based on different flow field designs. Current density flux magnitude indicated the consumption of reactants at relevant local areas.
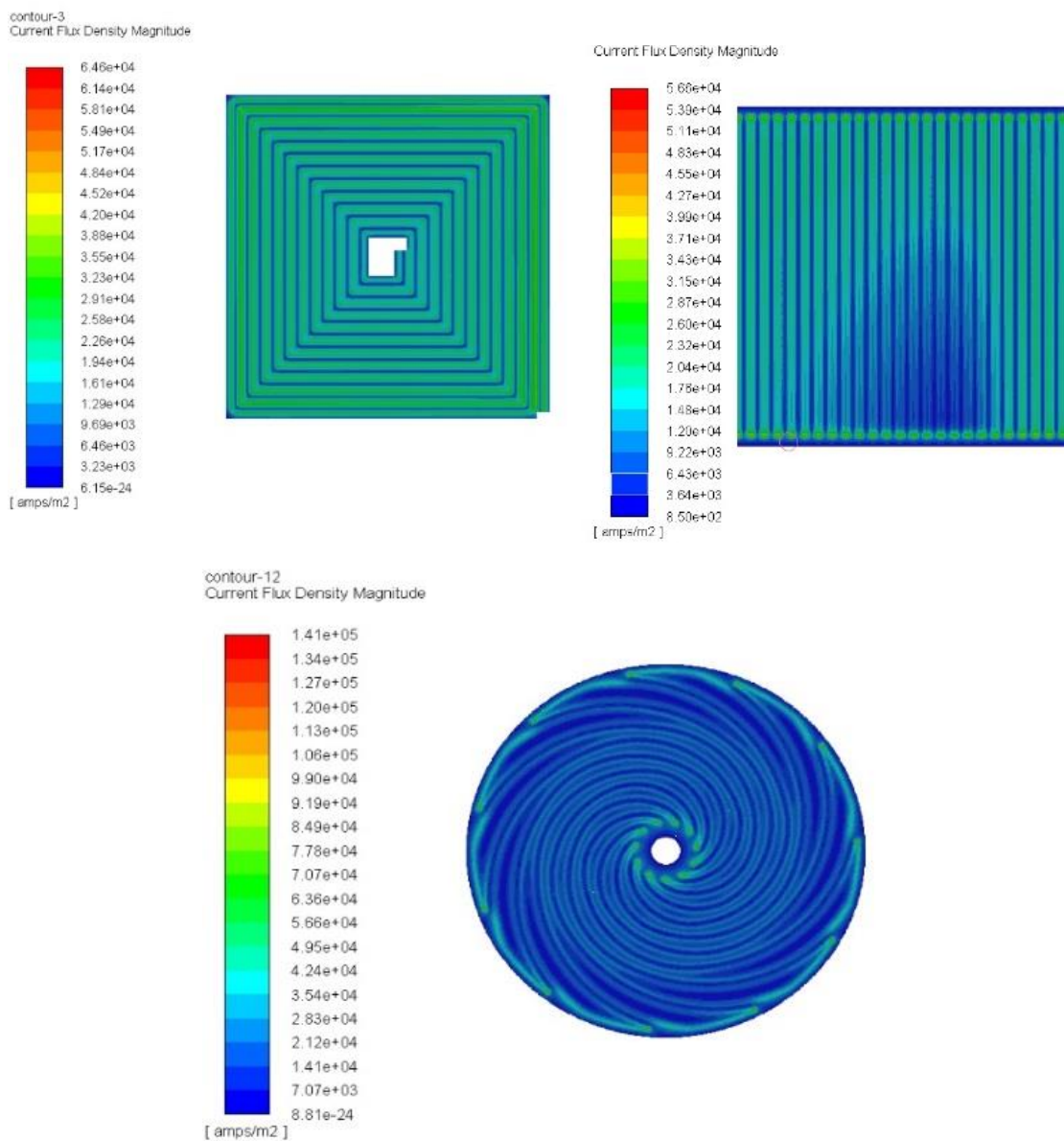
Figure 3.6. Current density distributions on the gas diffusion layer surface at 0.45 V

From simulation results, mostly uniform distribution of current density was obtained for Fibonacci spiral flow field while uniformity of current density distribution was the poorest in the conventional parallel design. Other parameters for performance was

also analyzed in detail by looking at different contours, including distributions of pressure,

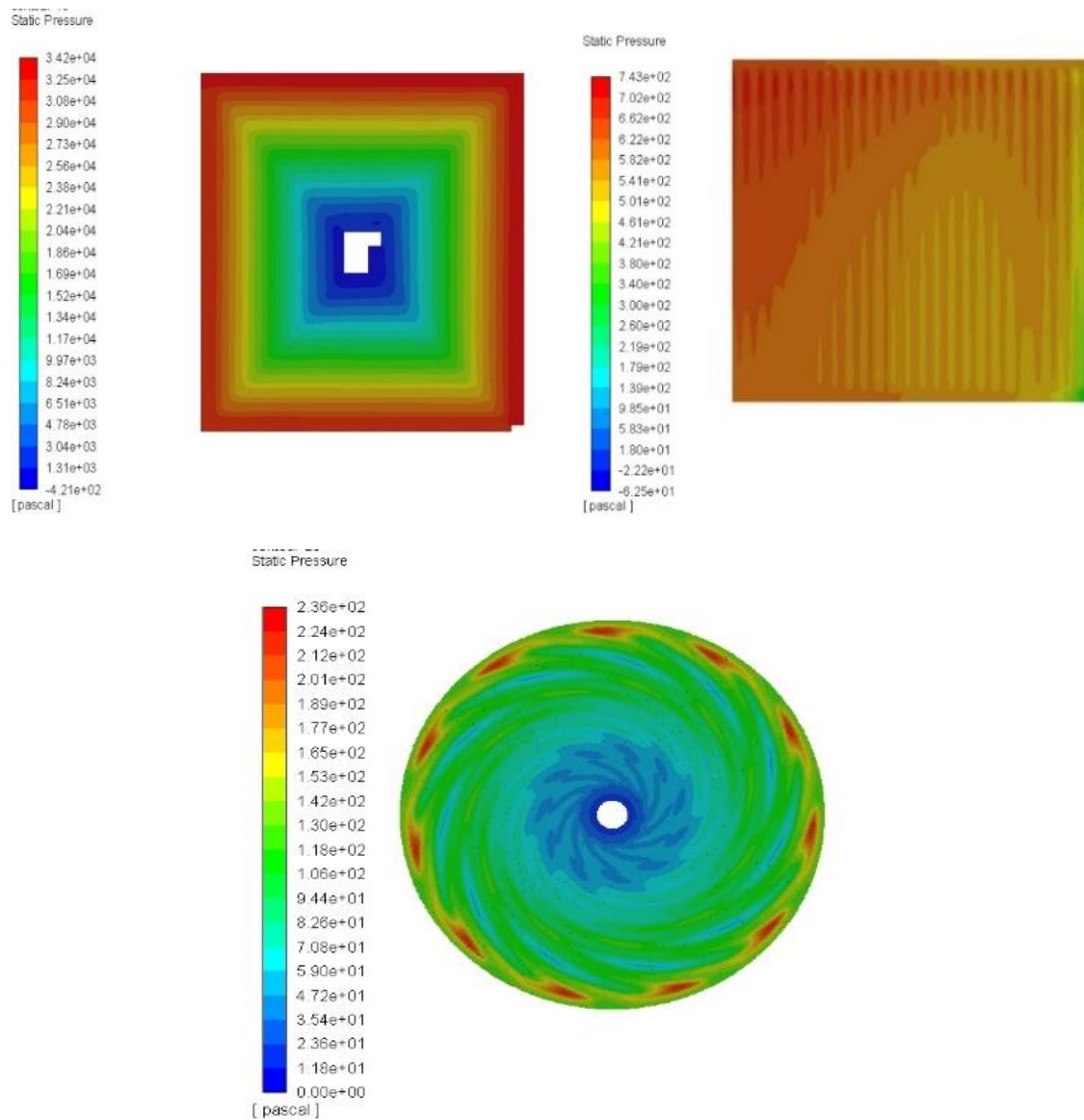velocity, reactants, concentration and water mass fraction.

Figure 3.7. Pressure distributions on cathode gas diffusion layer surface at 0.45 V

According to pressure distributions given in Figure 3.7., the pressure difference between maximum and minimum values, pressure drop, through cathode gas diffusion layer for rectangular spiral design, conventional parallel design, and Fibonacci spiral design were 34,000 Pa, 700 Pa, and 200 Pa, respectively. Much higher pressure drop was observed at the cathode side than anode side because oxygen gas has higher flow rates, higher density, and lower diffusivity compared to hydrogen gas [11]. Pressure drop through anode gas diffusion layer for rectangular spiral design, conventional parallel design and Fibonacci spiral design were 3,300 Pa, 50 Pa, and 15 Pa, respectively. The pressure drop must be met by pressure value provided by the compressor to the reactant gases at the inlets in order to maintain flow in the fuel cell. Therefore, the required auxiliary power increases with an increase in pressure drop. Required compressor power, W_{comp} can be calculated from [31]:

$$W_{comp} = \frac{1}{\eta_{comp}} \ c_p \ T_0 \ [\frac{P_0 + \Delta P}{P_0}]^{\frac{\gamma-1}{\gamma}} - 1] \ \dot{m} \qquad (3.3)$$

Here, η_{comp} is the isentropic efficiency of compressor, c_p is the specific heat coefficient of reactant gases at constant pressure, T_0 and P_0 are the operation temperature and pressure, ΔP is the pressure drop at anode and cathode side, $\dot{m}$ is the mass flow rate at anode inlet and cathode inlet given in the Table 3.3, and γ is the specific heat ratio.

The ratio of maximum power output to required compressor power input caused by pressure drop for each flow field design were plotted in Figure 3.8. Maximum fuel cell power output per required compressor power values were approximately 900, 200, and 10 for Fibonacci spiral design, parallel design, and rectangular spiral design, respectively.
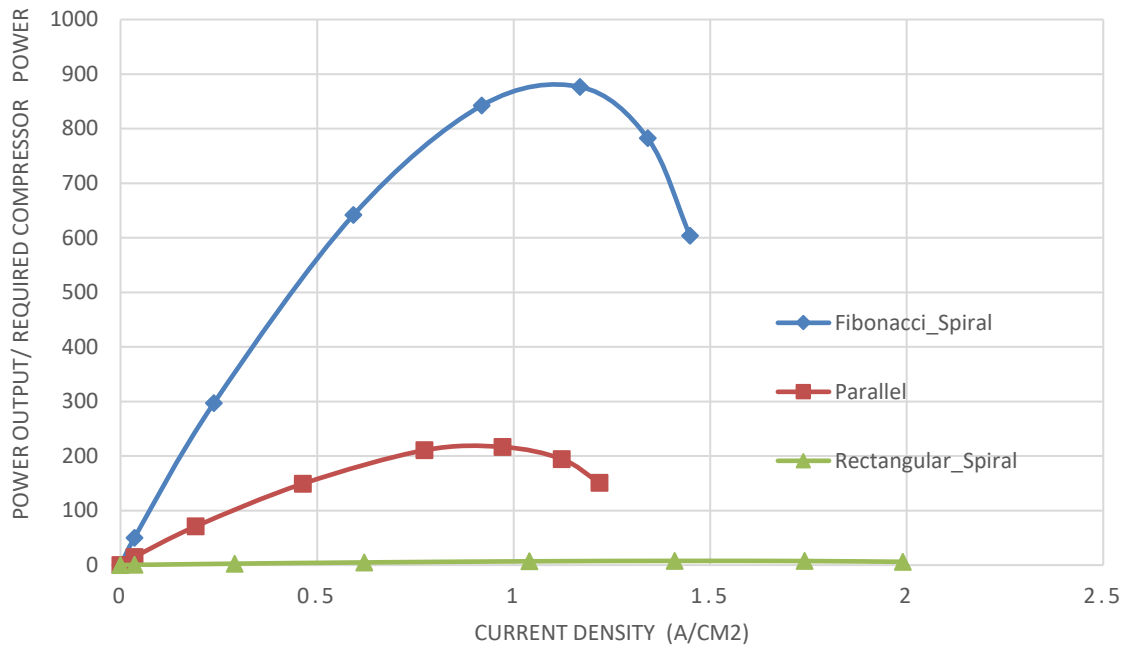
Figure 3.8. Fuel cell power output per required compressor power

Fuel cell power output per required compressor power values in fuel cell with Fibonacci spiral configuration was much larger than that of rectangular spiral design. Rectangular spiral design had one channel while parallel design had 25 channels and Fibonacci design had 11 channels as illustrated in Figure 3.2. Network between channels in Fibonacci spiral and parallel flow configurations are in parallel. In contrast, rectangular spiral design, which had much longer total channel length, is equivalent to pipes connected each other in series with respect to pressure drop calculation. Different network types between channels in rectangular spiral design and other flow field designs influence the overall pressure drop. In addition, rectangular spiral flow field had many corners with right

angles, giving rise to the pressure drop. On the other hand, pressure drop between adjacent channels caused convective flow under the rib. Convective flow's contribution on the gas transportation in addition to diffusion was higher due to high-pressure drop seen from inlet to outlet in the rectangular spiral design. In the design with Fibonacci spiral, pressure drop was significantly reduced by taking advantage spiral shape. Remarkably low pressure drop in the Fibonacci spiral design takes place during separation from wide circular inlet to thinner channels. There is symmetrical pressure distribution in the spiral designs in contrast to the parallel design.

Table 3.4. Comparison of O_2 molar concentration and velocity at cathode GDL-catalyst interface at 0.45 V

Flow Field Configuration	Average molar O_2 concentration $(kmol/m^3)$	Average O_2 gas velocity (m/s)	Max.O_2 molar concentration $kmol/m^3$	Max.O_2 gas velocity m/s
Conventional Parallel Design	0.00132	0.00117	0.00482	0.0041
Fibonacci-Spiral Design	0.00148	0.00159	0.00479	0.00304
Rectangular Spiral Design	0.00170	0.02289	0.00660	0.040

Experimental studies conducted by Chen et al. [8] showed the ratio of the convective flow under the rib to the diffusive flow based on the pressure drop between inlet channel and outlet channel. More convective flow was seen at a flow field design with non-interdigitated flow field configuration compared to the interdigitated design with dead-end channels. Rectangular spiral design had higher velocity values as given in Table 3.4 caused by the convective flow under the rib since it had much higher pressure drop.
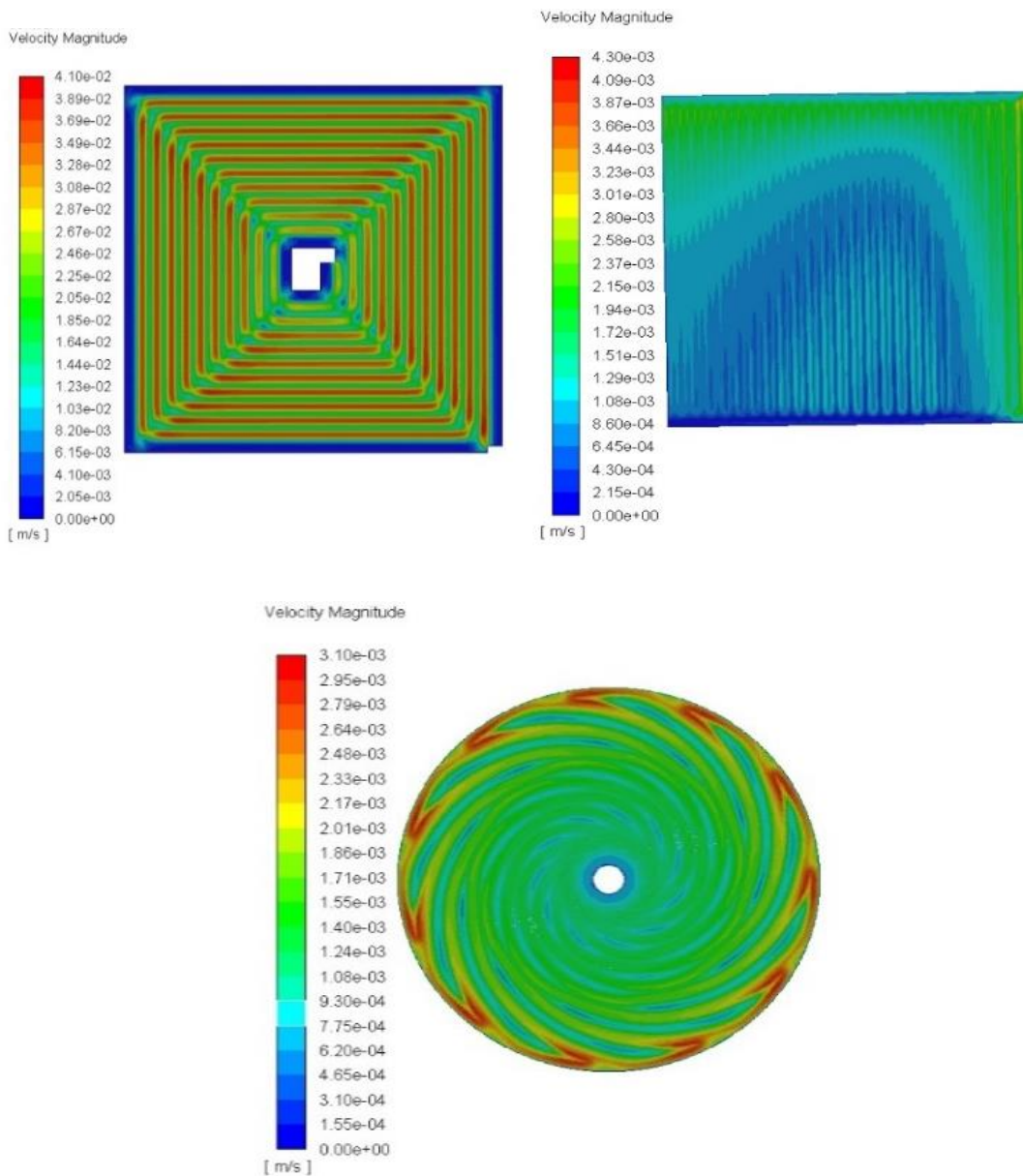
Figure 3.9. Velocity magnitude distributions at the cathode catalyst-GDL interface

Centrifugal force from inner to outer affected the flow within the PEMFC with the Fibonacci spiral design [30]. Even though centrifugal force had retarding influence over the flow in Fibonacci spiral design compared to conventional parallel design, Fibonacci

Rectangular spiral and Fibonacci spiral designs had symmetric oxygen molar concentration, as illustrated in Figure 3.10. Rectangular spiral design required high inlet pressure provided by auxiliary system to maintain reactant flow inside the fuel cell. High inlet pressure directly raised inlet reactant concentrations and accordingly generated more current density [9]. Therefore, rectangular spiral design showed highest molar oxygen concentration values. However, high reductions seen in molar oxygen concentration within the rectangular spiral channel from outer to inner could elevate thermal stress in such regions because of different rates of chemical reactions. Possibility of formation of this thermal stress was lower at Fibonacci spiral design because of lower concentration difference between its adjacent channels. In addition, symmetric distribution seen in the Fibonacci spiral design facilitated balancing of any thermal stress. These results imply that the Fibonacci spiral design to be more durable compared to the other PEMFC flow designs.

Mass fraction of water represents the water content in the vapor form. Reactants are humidified before supplied to cathode and anode channel inlets. Condensation from vapor to liquid can take place. The areas with relatively high water mass fraction have higher possibility to be covered by liquid water, which blocks the pore volume of gas diffusion layer. Due to this obstruction of reactant distribution through diffusion and convective flow from channel to catalyst layer, liquid water in the porous zone is unwanted in a PEMFC. The zones having high mass fraction of water value were more close to the outlet in the spiral channels compared to the parallel channels (Figure 3.11.). As a result, liquid water could be easily removed from outlet in the spiral design.
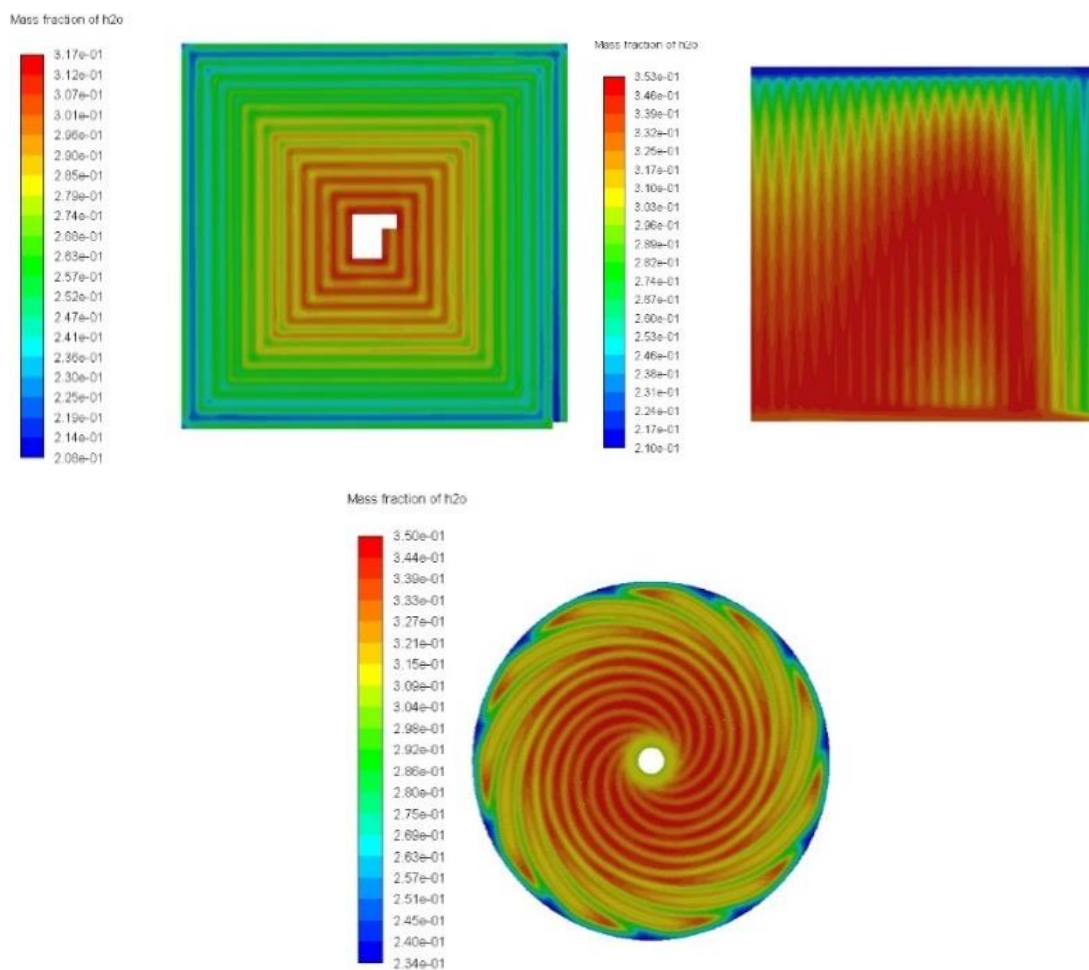
Figure 3.11. Mass fractions of water at cathode GDL

Consequently, water removal could be managed more effectively by Fibonacci spiral and rectangular spiral designs. Presence of noticeable relationship between pressure distribution and water mass fraction at cathode gas diffusion layer is worth to reinforce. When the simulation results related to pressure given in Figure 3.7 and mass fraction of water given in Figure 3.11 are considered together, the fact that water is transported from the area with high pressure to the area with lower pressure is realized.

4. SUMMARY AND CONCLUSIONS

Flow field design is one of the most important factors that affects the fuel cell performance. Uneven reactant distribution, low durability, and weak water management are main problems to be overcome in a PEMFC. However, these problems can be alleviated by designing proper flow fields. For this purpose, a nature-inspired flow field seen from hurricanes to seashells, namely Fibonacci spiral configuration, was applied to the flow channel design for a polymer electrolyte membrane fuel cells. Computational studies were conducted to investigate the performance of Fibonacci spiral design by comparing its performance with that of rectangular spiral design and conventional parallel design.

According to the detailed computations presented in this thesis, Fibonacci spiral design had slightly lower power output than the rectangular spiral channel as can be seen in the polarization and power density curves. However, the pressure drop in flow channels with the Fibonacci spiral design was much lower than that of rectangular spiral design and nearly the same with the conventional parallel design. Consequently, auxiliary power requirement for the Fibonacci spiral design to maintain flow was much less than those of other two designs. In other words, fuel cell power output per pumping power input for Fibonacci spiral design was much higher compared to the other two designs.

Centrifugal forces against flow direction and unstable ratio of channel width to rib width were two non-negligible additional effects on reactant velocity distribution in the Fibonacci spiral design. Uniform and high-speed reactant flow was observed in the Fibonacci spiral flow field. Because of the homogeneity seen in reactant concentration

distributions through active reaction area, electrochemical reactions took place with similar rates in Fibonacci spiral design. Therefore, the design considered in this study had lower possibility of thermal stress since similar electrochemical reaction rate through active area occurred. Thus, higher durability is expected from a PEMFC with Fibonacci spiral flow field compared to the conventional parallel and rectangular spiral designs.

Furthermore, Fibonacci spiral design had better water removing ability since the possibility of formation of liquid water was higher in areas near the outlet. Thereby, water could be removed without preventing reactant flow in this nature-inspired geometry. As a result, when all these advantages observed in the present computations were taken into consideration, Fibonacci spiral design clearly showed significantly better water-management ability compared to the conventional parallel and rectangular spiral designs.

Finally, Fibonacci spiral design's cost and manufacturing time are expected to become reasonable with the advanced manufacturing technologies although fabrication of flow channels with Fibonacci spiral design seems costly and time consuming. Also, advantages of Fibonacci spiral design might be enhanced with further optimization studies that take into consideration of the impact of other geometric parameters of the flow field design, such as shape of the cross section, channel depth, number of channels, and use of baffles in the flow field on the performance in the near future.

REFERENCES

[1]   J.Wang, H.Wang, Discrete approach for flow field designs of parallel channel configurations in fuel cells, International Journal Of Hydrogen Energy 37 (14) (2012) 10881–10897. doi:10.1016/j.ijhydene.2012.04.034.

[2]   H.-W.Wu, A review of recent development: Transport and performance modeling of PEM fuel cells, Applied Energy 165 (2016) 81–106.

[3]   J. Wang, H. Wang, Flow-field designs of bipolar plates in PEM fuel cells: Theory and applications, Fuel Cells 12 (6) (2012) 989–1003.

[4]   A.Aiyejina,M.K.S. Sastry, PEMFC flow channel geometry optimization: A review, Journal of Fuel Cell Science and Technology 9 (2012) 011011-1.

[5]   A.P.Manso, F.Fernandez., J.Barranco, X.Garikano,M.G.Mujika, Influence of geometric parameters of the flow fields on the performance of a PEM fuel cell: A review International Journal of Hydrogen Energy 37 (20) (2012) 15256-15287.

[6]   S.Meenakshi, P.C. Ghosh, Study of an innovative versatile flow design suitable for fuel cells, Journal of Electrochemical Energy Conversion and Storage 14 (4) (2017) 041003-041003-7. doi: 10.1115/1.4037391.

[7]   S.Alrwashdeh, I.Manke, H.Markötter, J.Haußmann, N.Kardjilov, A.Hilger, M.J.Kermani, M.Klages, A.M.Al-Falahat, J.Scholta, J. Banhart, Neutron radiographic in operando investigation of water transport in polymer electrolyte membrane fuel cells with channel barriers, Energy Conversion and Management 148 (2017) 604-610.

[8]   S.Chen, X.Zhang, H.Liu, Effect of pressure difference between adjacent channels in an adjustable flow field in PEM fuel cells, International Journal of Hydrogen Energy 42 (7) (2017) 4667-4672.

[9]   J.Heck, Decoupling pressure and distribution effects on the performance of polymer electrolyte fuel cells, Master Thesis, Missouri University of Science and Technology, 2017.

[10]   J.Kloess, X.Wang, J.Liu, Z.Shi, L.Guessous, Investigation of bio-inspired flow channel designs for bipolar plates in proton exchange membrane fuel cells, Journal of Power Sources 188 (2009) 132-140.

[11]   A.Arvay, J.French, J.C.Wang, X.-H.Peng, A.M.Kannan, Modelling and simulation of biologically inspired flow field design for proton exchange membrane fuel cells, The Open Electrochemistry Journal 6 (2015) 1-9. doi:10.2174/1876505X01506010001.

[12]   R.Roshandel, F.Arbabi, G.K.Moghaddam, Simulation of an innovative flow field design based on a bio inspired pattern for PEM fuel cells, Renewable Energy 41 (2012) 86-95. doi: 10.1016/j.renene.2011.10.008.

[13]   N.Guo, M.C.Leu, U.O.Koylu, Bio-inspired flow field designs for polymer electrolyte membrane fuel cells, International Journal of Hydrogen Energy 39 (2014) 21185-21195. doi: 10.1016/j.ijhydene.2014.10.069.

[14]   C. D. Murray, The physiological principle of minimum work in the vascular system and the cost of blood volume, Proceedings of the National Academy of Science 12 (1926) 207–214.

[15]   M.Asadzade, A.Shamloo, Design and simulatiom of a novel bipolar plate based on lung-shaped bio-inspired flow pattern for pem fuel cell, International Journal of Energy Research 41 (2017) 1730-1739. doi:10.1002/er.3741.

[16]   B.Saripella,U.O.Koylu,M.C.Leu, Experimental and computational evaluation of performance and water management characteristics of a bio-inspired proton exchange membrane fuel cell, Journal of Fuel Cell Science and Technology 12 (6) (2015) doi: 10.1115/1.4032041.

[17]   C.E.Damian-Ascencio, A.Saldana-Robles, A.Hernandez-Guerrero, Numerical modelling of a proton exchange membrane fuel cell with tree-like flow field channels based on an entropy generation analysis, Energy 133 (2017) 306-316.

[18]   Ramos-Alvarado B, Hernandez-Guerrero A, Elizalde- Blancas F, Ellis MW. Constructal flow distributor as a bipolar plate for proton exchange membrane fuel cells. International Journal of Hydrogen Energy 36 (2011) 12965-12976.

[19]   Ansys academic research,release 18.0,help system,fuel cell modules manuel.

[20]   A.Arvay,Proton exchange membrane fuel cell modelling and simulation using Ansys Fluent, Master Thesis,Arizona State Uiversity, 2011.

[21]   C.Hsu,J.Jiang,H.Dang,T.Nguyen, Investigating the design parameters on spiral micro-channel by using fibonacci sequence and taguchi method, Microsystem Technologies 24 (2016) 255-271.

[22]   A.Benovali,L.Chisci,A.Farina,Fibonacci sequence, golden section, kalman filter and optimal control, Journal of Signal Processing 89 (2009)1483-1488.

[23]   R.O'Hayre, S.-W.Cha, W.Colella, F.B.Prinz, Fuel Cell Fundementals,2nd Edition, John Wiley&Sons, 2009.

[24]   F.Alejandro, Polymer electrolyte fuel cells: Science, applications and challenges, CRC Press, Boca Raton,2013.

[25]   S.Cano-Andrade,A.Hernandez-Guerrero,M.R.Spakovski,C.E.Damian-Ascencio,J.C.Rubio-Arana, Current density and polarization curves for radial flow field patterns applied to PEMFCs (proton exchange membrane fuel cells),Energy 35 (2010) 920-927.

[26]   D.Juarez-Robles,A.Hernandez-Guerrero,B.Ramos-Alvarado,Multiple concentric spirals for the flow field of a proton exchange membrane fuel cell, Journal of Power Science 196 (2011) 8019-8030.

[27]   A.Iranzo, M.Munoz, F.Rosa, J.Pino, Numerical model for the performance prediction of a pem fuel cell. model result and experimental validation, International Journal of Hydrogen Energy 35 (20) (2010) 11533-11550.

[28]   W. Lidwell, K.Holden, J. Butler, Universal principles of design: A cross-disciplinary   reference, Gloucester MA: Rockport Publishers, 2003.

[29]   J. Hambidge, Dynamic symmetry: The Greek Vase, New Haven CT, Yale University Press, 1920.

[30]   T.Monsaf, B.Hocine, S.Youcef, M.Abdallah, Unsteady three-dimensional numerical study of mass transferring pem fuel cell with spiral flow field, International Journal of Hydrogen Energy 42 (2017) 1237-1251.

[31]   A.Dicks, J.Larminie, Fuel Cell Systems Explained, 2nd Edition, John Wiley&Sons, 2003.

[32]   I.Khazaee,M.Ghazikhani,Performance improvement of proton exchange membrane fuel cell by using annular shaped geometry,Journal of Power Sources 196 (5) (2011) 2661-2668.

VITA

Suleyman Kose received his B.Sc. (with honors) degree in Mechanical Engineering from Yildiz Technical University, Turkey in 2013. In July 2018, he received his Master of Science degree in Mechanical Engineering from Missouri University of Science and Technology, Rolla, Missouri.